Mg-Doped Na₄Fe₃(PO₄)₂(P₂O₇)/C Composite with Enhanced Intercalation Pseudocapacitance for Ultra-Stable and High-Rate Sodium-Ion Storage

Fangyu Xiong, Jiantao Li, Chunli Zuo, Xiaolin Zhang, Shuangshuang Tan, Yalong Jiang, Qinyou An,* Paul K. Chu, and Liqiang Mai*

Na$_4$Fe$_3$(PO$_4$)$_2$(P$_2$O$_7$) (NFPP) is considered as a promising cathode material for sodium-ion batteries (SIBs) due to its low cost, non-toxicity, and high structural stability, but its electrochemical performance is limited by the poor electronic conductivity. In this study, Mg-doped NFPP/C composites are presented as cathode materials for SIBs. Benefiting from the enhanced electrochemical kinetics and intercalation pseudocapacitance resulted from the Mg doping, the optimal Mg-doped NFPP/C composite (NFPP-Mg5%) delivers high rate performance (capacity of ≈40 mAh g^{-1} at 20 A g^{-1}) and ultra-long cycling life (14 000 cycles at 5 A g^{-1} with capacity retention of 80.8%). Moreover, the in situ X-ray diffraction and other characterizations reveal that the sodium storage process of NFPP-Mg5% is dominated by the intercalation pseudocapacitive mechanism. In addition, the full SIB based on NFPP-Mg5% cathode and hard carbon anode exhibits the discharge capacity of ≈50 mAh g^{-1} after 200 cycles at 500 mA g^{-1}. This study demonstrates the feasibility of improving the electrochemical performance of NFPP by doping strategy and presents a low-cost, ultra-stable, and high-rate cathode material for SIBs.

1. Introduction

The development of renewable energy such as solar, wind and tidal energy is of great significance for achieving a sustainable human society.[1,2] Considering the intermittency of these energy sources, establishing smart grids based on large-scale energy storage systems (LSESSs) is vital for realizing their efficient utilization.[3,4] Sodium-ion batteries (SIBs) are considered as a promising choice for LSESSs owing to the low cost, high abundance, and wide distribution of sodium resources.[5–7] However, although many efforts have been devoted to the development of SIBs, it remains a challenge to obtain high-performance and low-cost cathode materials for SIBs that meet the requirements of LSESSs.

Inspired by the great successful of LiFePO$_4$ in LIBs, many researchers have paid attention to Fe-based phosphates as cathode materials for SIBs.[8,9] Moreover, Fe-based phosphates possess the advantages of low cost, high abundance, non-toxicity, and high structural stability.[10,11] Unfortunately, different from LiFePO$_4$, the thermodynamically favorable NaFePO$_4$ is maricite structure without Na-ion diffusion channels, thus it displays low electrochemical activity as cathode materials for SIBs.[12–14] Therefore, many researchers transfer attention to other Fe-based phosphates, such as Na$_2$FeP$_2$O$_7$,[15,16] Na$_2$FePO$_4$F,[17,18] Na$_3$Fe$_2$(PO$_4$)$_3$,[19,20] and so forth.[21,22] Among these, Na$_4$Fe$_3$(PO$_4$)$_2$(P$_2$O$_7$) (NFPP) exhibits relatively high operating potential (≈3.1 V vs Na$^+$/Na) and theoretical capacity (129 mAh g^{-1}), and low volume change (≈4%).[23,24] Furthermore, NFPP has 3D Na-ion diffusion channels, which is beneficial for realizing high-rate capability.[25] Although NFPP shows great potential, its practical electrochemical performance is unsatisfied due to the poor electronic conductivity.[26–29] Therefore, various NFPP/C composites have been fabricated to modify the electronic transport and achieve enhanced electrochemical performance.[9,28–32] However, fabricating NFPP/C composites only can facilitate the electronic transport outside NFPP particles, but cannot change its own conductivity, i.e., the electronic conductivity inside particles is still poor. Doping is identified as an efficient approach to

F. Xiong, J. Li, C. Zuo, S. Tan, Y. Jiang, Q. An, L. Mai
State Key Laboratory of Advanced Technology for Materials Synthesis and Processing
Wuhan University of Technology
Wuhan 430070, P. R. China
E-mail: anqinyou86@whut.edu.cn; mlq518@whut.edu.cn
F. Xiong, X. Zhang, P. K. Chu
Department of Physics
Department of Materials Science and Engineering
and Department of Biomedical Engineering
City University of Hong Kong
Tat Chee Avenue, Kowloon, Hong Kong 999077, P. R. China
S. Tan
College of Materials Science and Engineering
Chongqing University
Chongqing 400030, P. R. China
Q. An, L. Mai
Hubei Longzhong Laboratory
Wuhan University of Technology (Xiangyang Demonstration Zone)
Xiangyang, Hubei 441000, P. R. China

improve the electronic conductivity of materials by introducing impurity energy levels and has been widely used in various electrode materials for rechargeable batteries.[33–35] Therefore, fabricating the doping modified NFPP/C composites holds high promise to realize fast electron transport both outside and inside NFPP particles, thereby achieving superior electrochemical performance, but related report is still rare.

Herein, Mg-doped NFPP/C composites were presented and evaluated as cathode materials for SIBs. Mg was chosen as dopant because of its high abundance, low molar mass, and similar ionic radius (0.72 Å) with high-spin Fe^{2+} (0.78 Å).[36–38] Moreover, the positive role of Mg doping in some other cathode materials for SIBs was confirmed.[39–41] In this work, compared to undoped NFPP/C composite (NFPP-0), the 5% Mg doped NFPP/C composite (NFPP-Mg5%) displays highly enhanced rate performance ($\approx$40 mAh g^{-1} at 20 A g^{-1}) and ultra-long cycling life (14 000 cycles at 5 A g^{-1} with capacity retention of 80.8%). The role of Mg doping was revealed by the electrochemical kinetic analysis and the sodium storage mechanism was investigated by the in situ X-ray diffraction (XRD), ex situ X-ray photoelectron spectroscopy (XPS), and electrochemical analysis. The enhanced electrochemical kinetics and intercalation pseudocapacitance of NFPP-Mg5% are demonstrated as the origin for the enhanced rate performance and ultra-long cycling life.

Besides, the full SIBs based on NFPP-Mg5% were assembled and display good electrochemical performance, which further demonstrates the application potential of NFPP-Mg5%.

2. Results and Discussion

The XRD patterns of NFPP-0, NFPP-Mg5%, and NFPP-Mg10% (Figure S1, Supporting Information) are similar and match well with the previously reported NFPP (orthorhombic, space group: $Pn2_1a$),[23] indicating that replacing 5% or 10% of Fe by Mg only makes slight change on the crystal structure. Some diffraction peaks slightly shift to higher angle after Mg doping (Figure S1, Supporting Information), indicating the decrease of cell parameters. Moreover, the Rietveld refinements of XRD patterns of NFPP-0 and NFPP-Mg5% were performed to further compare the difference in crystal structure of NFPP before and after Mg doping (**Figure 1**a; Figure S2, Supporting Information). The Rietveld refinement results (Table S1, Supporting Information) show that the lattice parameters of NFPP shrink slightly after Mg doping. The slight shrinkage of lattice parameters is ascribed to the smaller ionic radius of Mg^{2+} (0.72 Å) compared to Fe^{2+} (0.78 Å), implying that the Mg dopant is successfully introduced into the crystal structure of NFPP. Moreover, the
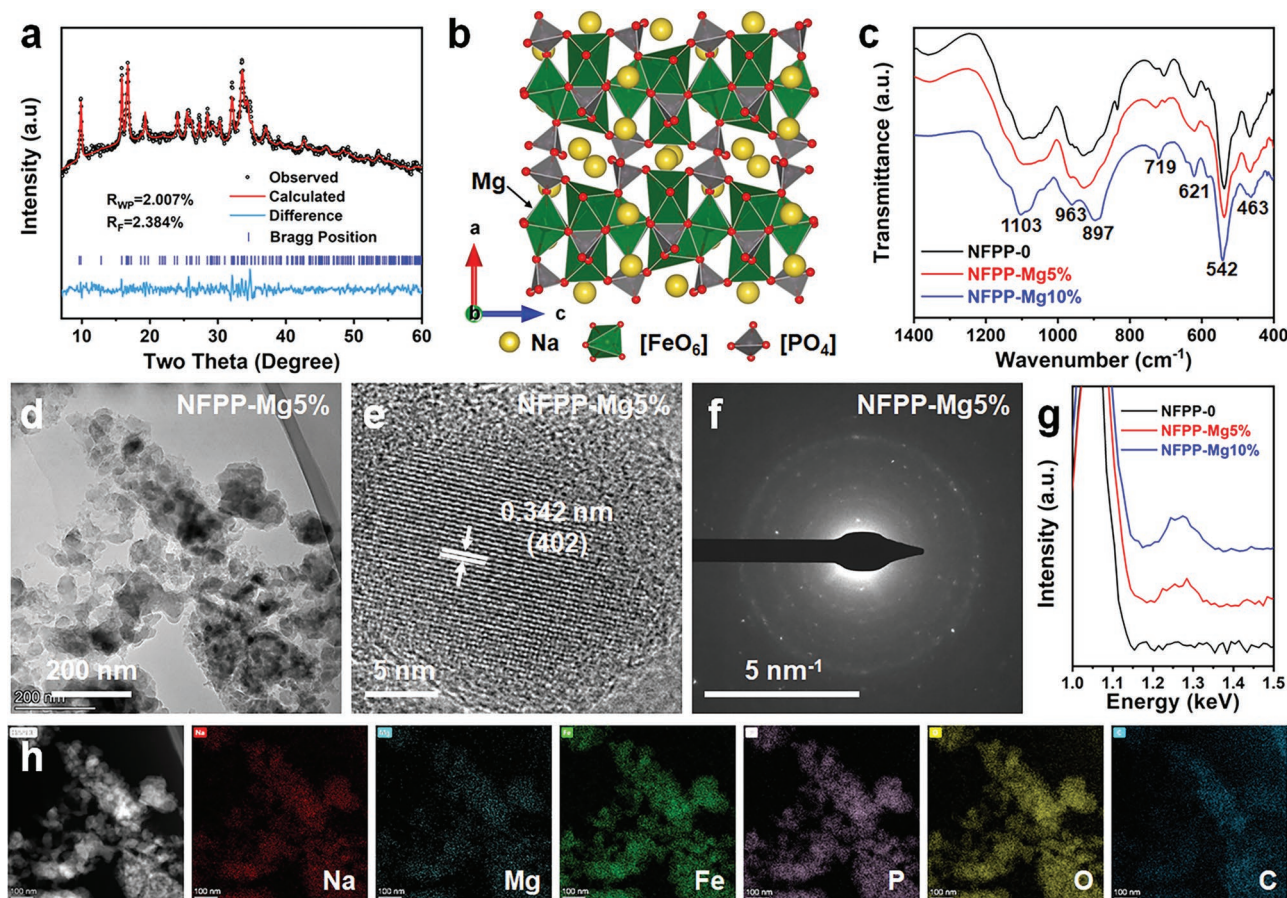
Figure 1. Materials characterizations. a) Rietveld refinement of XRD pattern of NFPP-Mg5%; b) Schematic for crystal structure of NFPP with Mg doping; c) FTIR spectra of NFPP-0 NFPP-Mg5%, and NFPP-Mg10%; d) TEM image, e) HRTEM image and f) SAED pattern of NFPP-Mg5%; g) EDS spectra of NFPP-0, NFPP-Mg5%, and NFPP-Mg10%; h) HADDF-STEM image and EDS elemental mappings of NFPP-Mg5%.

average length of Na—O bonds increases from 2.50 to 2.56 Å after Mg doping, facilitating the Na-ion diffusion.[41] In NFPP, the $[Fe_3P_2O_{13}]_\infty$ layers are linked by $[P_2O_7]$ units to form a 3D framework with large ionic channels (Figure 1b), which is benefit for realizing the fast sodium-ion diffusion.[23,42] The introduced Mg is expected to occupy on Fe site due to the similar radii of Mg^{2+} and high-spin Fe^{2+}. Moreover, Fourier transforms infrared (FTIR) spectroscopy was employed to study the bonding structure. In the FTIR spectra of three samples (Figure 1c), the peaks corresponding to the vibrations in the both PO_4 (450–650 cm^{-1} and 975–1200 cm^{-1}) and P_2O_7 (719 and 963 cm^{-1}) units are observed.[9,43] In the Raman spectra (Figure S3a, Supporting Information), the broad D and G bands at 1350 and 1590 cm^{-1}, respectively, demonstrate the existence of carbon in three samples.[44,45] Moreover, the Raman spectra of three samples in the Raman shift range from 900 to 1900 cm^{-1} can be deconvoluted into several peaks by fitting (Figure S3b–d, Supporting Information).[46,47] The bands at ≈1350 cm^{-1} (D) and 1590 cm^{-1} (G) are ascribed to the disordered graphitic lattice and ideal graphitic lattice, respectively.[46] The A (≈1500 cm^{-1}) and I (≈1200 cm^{-1}) bands are assigned to amorphous sp^2-bonded forms of carbon and the polyene-like structures, respectively.[48,49] In addition, the band at ≈1000 cm^{-1} is ascribed to the $[PO_4]^{3-}/[P_2O_7]^{4-}$ groups of NFPP.[50] The fiting D/G ratios of NFPP-0, NFPP-Mg5%, and NFPP-Mg10% are 1.19, 1.21, and 1.22, respectively. The similar D/G ratios demonstrate that the Mg doping has an ignorable effect on the graphitization degree of the carbon coating layer. Moreover, thermogravimetric (TG) analysis was employed to determine the carbon contents of three samples (Figure S4, Supporting Information). Meanwhile, in order to evaluate the composition of NFPP after the heating test, the XRD pattern of NFPP-0 after annealing at 600 °C in the air for 2 h was measured (Figure S5, Supporting Information). The XRD pattern indicates that the heated product of NFPP is composed of $Na_3Fe_2(PO_4)_3$ major phase (JCPDS 45–0319) and Fe_2O_3 secondary phase (JCPDS 86–0550). Therefore, the speculated reaction of NFPP during annealing in the air is described as the following equation:

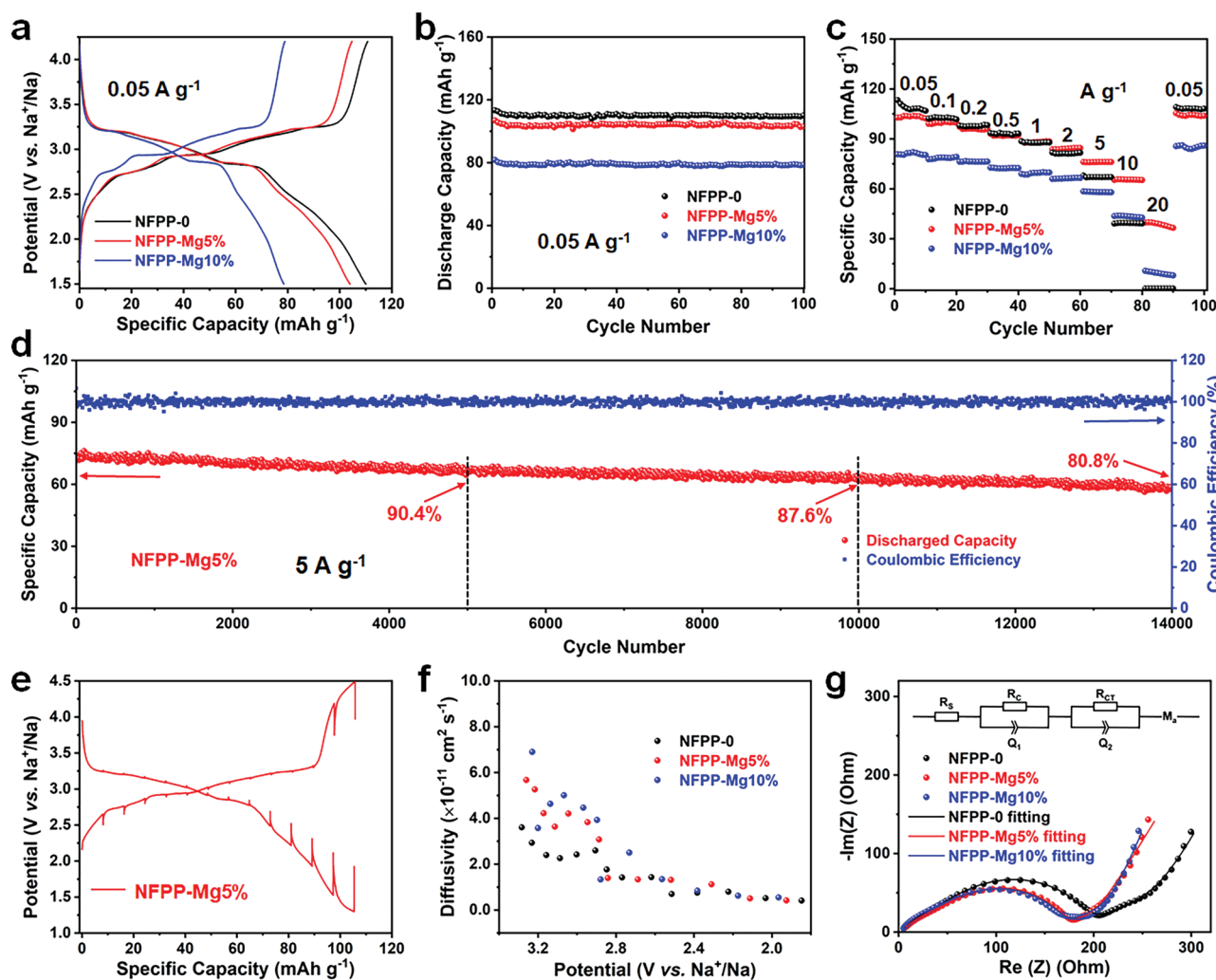$$12Na_4Fe_3(PO_4)_2(P_2O_7) + 9O_2 \rightarrow 16Na_3Fe_2(PO_4)_3 + 2Fe_2O_3 \quad (1)$$
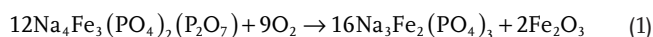
Based on this equation, the carbon contents of NFPP-0, NFPP-Mg5%, and NFPP-Mg10% were calculated to be 16.1%, 15.0%, and 14.2%, respectively. Besides, XPS was utilized to investigate the element composition and chemical state of NFPP-0, NFPP-Mg5%, and NFPP-Mg10% (Figure S6, Supporting Information). The Na, Fe, P, O, and C signals are detected in the survey XPS spectra of all three samples (Figure S6a, Supporting Information). Moreover, the Mg 1s peak is observed in Mg 1s XPS spectra of NFPP-Mg5% and NFPP-Mg10% but absent in that of NFPP-0 (Figure S6c, Supporting Information), indicating that the Mg element is successfully introduced in NFPP-Mg5% and NFPP-Mg10%. Besides, according to the inductively coupled plasma-atomic emission spectroscopy (ICP-AES) results, the Mg/Fe/P molar ratio of NFPP-0, NFPP-Mg5%, and NFPP-Mg10% are 0.00:3.11:4.00, 0.16:2.92:4.00, and 0.33:2.76:4.00, respectively, which are close to the expected values.

Scanning electron microscopy (SEM) and transmission electron microscopy (TEM) technologies were employed to investigate the morphology of NFPP-0, NFPP-Mg5%, and NFPP-Mg10%. The SEM (Figure S7, Supporting Information) and TEM images (Figure 1d; Figure S8a,b, Supporting Information) show that all the three samples are composed of irregular nanoparticles with size of below 200 nm. The lattice fringes corresponding to the (402) plane of NFPP were observed in the high-resolution TEM (HRTEM) image of NFPP-Mg5% (Figure 1e). In addition, the HRTEM images of NFPP-0, and NFPP-Mg10% (Figure S8c,d) display the lattice fringes that match well with the (210) and (011) planes of NFPP, respectively. The selected area electron diffraction (SAED) pattern of NFPP-Mg5% (Figure 1f) displays the polycrystalline feature of the nanoparticle aggregation. Besides, the energy dispersive spectroscopy (EDS) results (Figure 1g) demonstrate the existence of Mg element in NFPP-Mg5% and NFPP-Mg10%, but no Mg signal for NFPP-0. Moreover, the EDS elemental mappings (Figure 1h) show the even distribution of Na, Mg, Fe, P, and O in NFPP-Mg5% sample, implying that the Mg was introduced into the NFPP crystal rather than segregated to MgO or other Mg species alone.

To evaluate the effects of Mg doping on the sodium storage properties of NFPP, the cyclic voltammetry (CV) and galvanostatic charge/discharge tests of three samples were carried out. In the CV curves of NFPP-Mg5% at 0.1 mV s^{-1} (Figure S9b, Supporting Information), four couples of oxidation/reduction peaks at 2.83/2.46, 3.00/2.83, 3.20/3.11 and 3.28/3.19 V (vs Na^+/Na) are observed, implying the multi-step sodium-ion extraction/insertion process of NFPP. The oxidation peaks at 2.83 and 3.00 V are corresponding to the transformation of $Na_4Fe_3(PO_4)_2(P_2O_7)$ to $Na_2Fe_3(PO_4)_2(P_2O_7)$ with the extraction of Na-ion at Na3 (5-coordinated) and Na1 (6-coordinated) sites.[28,42] In addition, the oxidation peaks at 3.20 and 3.28 V are assigned to the transformation of $Na_2Fe_3(PO_4)_2(P_2O_7)$ to $NaFe_3(PO_4)_2(P_2O_7)$ with the extraction of Na-ion at Na4 site (6-coordinated).[28,42] The reduction peaks are assigned to the corresponding reverse processes. The CV curves of NFPP-0 (Figure S9a, Supporting Information) and NFPP-Mg10% (Figure S9c, Supporting Information) are similar with that of NFPP-Mg5%, indicating the similar multi-step sodium storage process of three samples. At 0.05 A g^{-1}, NFPP-Mg5% displays a reversible capacity of 104 mAh g^{-1}, which is slightly lower than that of NFPP-0 (110 mAh g^{-1}) because the introduced Mg-ion is electrochemically inactive in the potential range employed (**Figure 2**a). Moreover, the discharge curves of three samples deliver multiple plateaus in 2.75–3.25 V and slope below 2.5 V, which correspond well with the CV curves. In addition, three samples exhibit excellent cycling stability at 0.05 A g^{-1} (Figure 2b). Except for the slight decay in the first several cycles, the capacities of three samples remain stable in the 100 cycles. The rate performances of three samples are displayed in Figure 2c. Even at 20 A g^{-1}, the capacity of NFPP-Mg5% still remains ≈40 mAh g^{-1}, which is superior to that of NFPP-0 (≈0 mAh g^{-1}) and NFPP-Mg10% (≈10 mAh g^{-1}). The modified Peukert plots of three samples (Figure S10, Supporting Information) display that the NFPP-Mg5% exhibits highest capacity when the current density is over 1 A g^{-1}. More importantly, the capacity retention of NFPP-Mg5% is higher than that of NFPP-0 under all tested current

**ADVANCED
SCIENCE NEWS**

www.advancedsciencenews.com

**ADVANCED
FUNCTIONAL
MATERIALS**

www.afm-journal.de

Figure 2. Electrochemical performance. a) Charge/discharge profiles and b) cycling performance of NFPP-0, NFPP-Mg5%, and NFPP-Mg10% at 0.05 A g^{-1}; (c) Rate performance of NFPP-0, NFPP-Mg5%, and NFPP-Mg10%; d) Long-term cycling performance of NFPP-Mg5% at 5 A g^{-1}; (e) GITT curves of NFPP-Mg5%; f) The Na-ion diffusivities of NFPP-0, NFPP-Mg5%, and NFPP-Mg10% during discharge process calculated from GITT test; g) EIS plots and equivalent circuit fitting results of NFPP-0, NFPP-Mg5%, and NFPP-Mg10% after 3 cycles at 0.05 A g^{-1} and the equivalent circuit model (insert).

densities (Figure S11, Supporting Information). Meanwhile, the corresponding charge–discharge curves of three samples (Figure S12, Supporting Information) show that NFPP-Mg5% displays smaller overpotential compared to NFPP-0 and NFPP-Mg10%, especially at high current densities. These results demonstrate that the suitable amount of Mg doping plays positive role on the rate performance of NFPP. In addition, the rate performance of NFPP-Mg5% is superior to many reported NFPP-based cathode materials for SIBs (Table S2, Supporting Information).[9,25–32,42,50,51] In order to investigate the effect of carbon content, the bare NFPP and NFPP-0 with lower carbon content (denoted as NFPP-0-LC) were synthesized. However, the XRD pattern (Figure S12a, Supporting Information) indicates that the synthesis of bare NFPP failed. The XRD pattern of NFPP-0-LC (Figure S12b, Supporting Information) is match well with NFPP. Based on the TG plot (Figure S12c, Supporting Information), the carbon content of NFPP-0-LC was calculated as 9.41%. Compared to NFPP-0, NFPP-0-LC displays inferior

rate performance (Figure S12d, Supporting Information), demonstrating the carbon is beneficial for achieving better electrochemical performance. This indicates that the high carbon content is responsible for the good electrochemical performance of NFPP-0 and the excellent electrochemical performance of NFPP-Mg5% is attributed to the synergistic effect of carbon coating and Mg doping. Furthermore, the long-term cycling stability of NFPP-Mg5% was evaluated (Figure 2d). After 14 000 cycles at 5 A g^{-1}, a capacity retention of 80.8% is still remained. To the best of our knowledge, this is the longest cycling life for the reported NFPP-based cathode materials for SIBs (Table S2, Supporting Information).[9,25–32,42,50,51] These results demonstrate that combining carbon coating and doping is an promising strategy to obtain high-performance NFPP-based cathode materials.

In order to reveal the origin for the enhanced rate performance of NFPP-Mg5%, galvanostatic intermittent titration technique (GITT) and electrochemical impedance spectroscopy

(EIS) were utilized to analyze the electrochemical kinetics of NFPP-0, NFPP-Mg5%, and NFPP-Mg10% samples. During the GITT test, NFPP-0, NFPP-Mg5%, and NFPP-Mg10% display discharge capacities of 110, 104, and 78 mAh g^{-1}, respectively (Figure 2e; Figure S14, Supporting Information). Based on the GITT test, the sodium-ion diffusivities were calculated (the detailed calculation method are displayed in Figure S15 and Table S3, Supporting Information). During the discharge process, the calculated sodium-ion diffusivities of three samples exhibit similar decrease trend (Figure 2f). In the potential range of main discharge plateaus (2.6–3.3 V vs Na$^+$/Na), the Mg-doped samples (NFPP-Mg5% and NFPP-Mg10%) display higher sodium-ion diffusivities than pristine one (NFPP-0), demonstrating that the Mg doping enhances the sodium-ion diffusion in NFPP. Specifically, the average sodium-ion diffusivities of NFPP-0, NFPP-Mg5%, and NFPP-Mg10% are 1.72×10^{-10}, 2.77×10^{-10}, and 2.97×10^{-10} cm^2 s^{-1}, respectively, which are similar to the previously reported results.[28–31] In the EIS plots (Figure 2g), NFPP-Mg5% and NFPP-Mg10% display smaller semicircle compared to NFPP-0, implying that the lower charge transfer resistance (R_{CT}) is obtained after Mg doping. To further compare the R_{CT} of three samples, the EIS plots were fitted using an equivalent circuit model (insert of Figure 2g). In the model, R_S, R_C, and R_{CT} are solution (electrolyte) resistance, contact resistance and charge transfer resistance, respectively. M$_a$ is the "modified restricted diffusion" element, and R_{Ma}, one parameter of Ma, is related to the resistance of solid-state diffusion.[52–56] The fitting results (Table S4, Supporting Infor-

mation) show that the R_{CT} of NFPP-Mg5% is 92.2 Ω, which is lower than that of NFPP-0 (123.1 Ω). Meanwhile, NFPP-Mg5% delivers a lower R_{Ma} (102.2 Ω) compared to NFPP-0 (220.6 Ω). Moreover, the electronic conductivities of NFPP-0 and NFPP-Mg5% calculated from I–V plots (Figure S16, Supporting Information) are 1.24×10^{-4} S m^{-1} and 1.73×10^{-4} S m^{-1}, respectively, demonstrating the positive effect of Mg doping on the electronic conductivity. These results indicate that the suitable Mg doping can improve both the electronic conductivity and Na-ion solid-state diffusion kinetics of NFPP, which is responsible for the enhanced rate performance of NFPP-Mg5%.

Furthermore, in situ XRD and ex situ XPS technologies were employed to understand the sodium storage mechanism of NFPP-Mg5%. The in situ XRD patterns of NFPP-Mg5% during first charge/discharge process and corresponding potential-time profiles are displayed in **Figure 3**a. In the first charge process, the (022), (222), and (602) diffraction peaks of NFPP-Mg5% shift to higher angle, indicating the lattice shrink during the sodium-ion extraction process. Notably, the (004) diffraction peak first shifts to lower angle then to higher angle in the charge process, confirming that the cell parameter *c* first increases and then decreases. This is attributed to the significant distortion of [P$_2$O$_7$] unit in NaFe$_3$(PO$_4$)$_2$(P$_2$O$_7$), which leads to the shift of Fe1 site along the *a* direction, reducing the cell parameter *c*. This phenomenon agrees with the structural evolution of NFPP during charge process reported in the previous literatures.[24,42] In the subsequent discharge process, the inverse change was observed, proving the high reversibility. Moreover, only peak
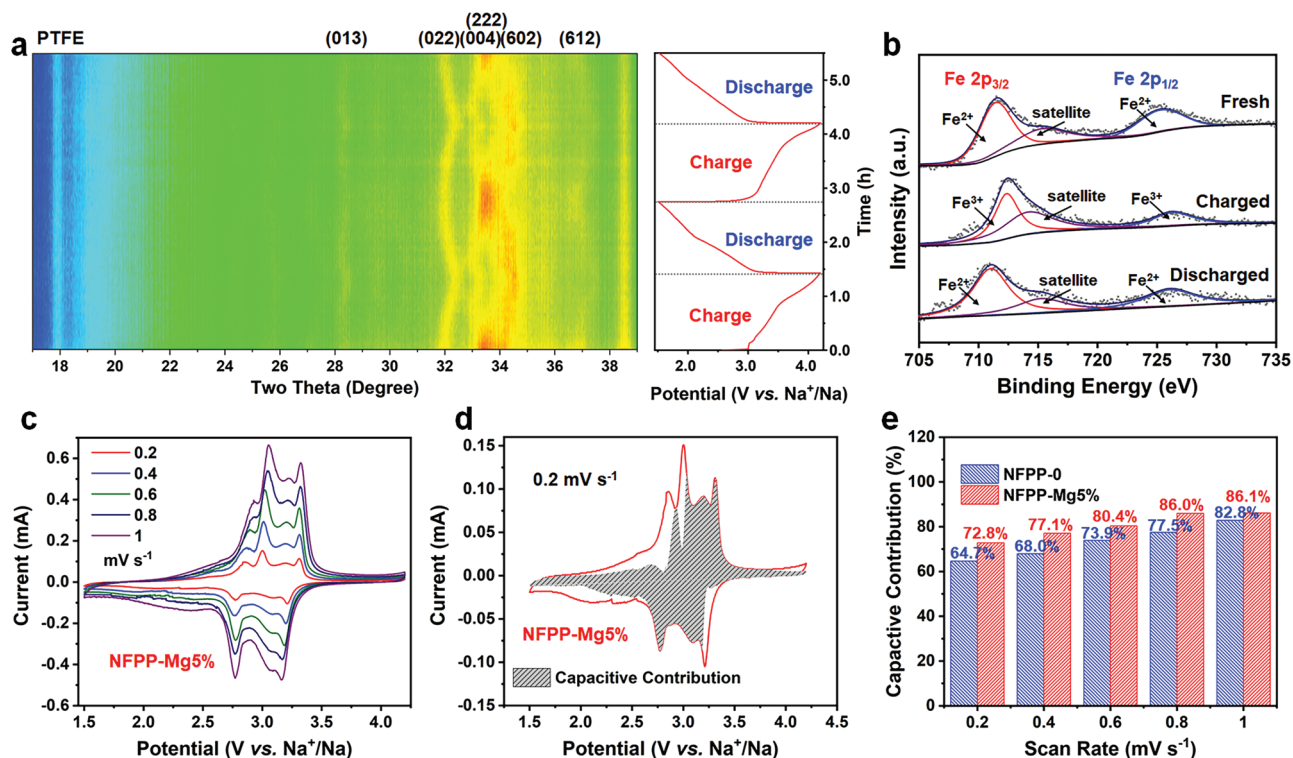
Figure 3. Sodium storage mechanism. a) In situ XRD patterns and corresponding potential-time plot of NFPP-Mg5%; b) Fe 2p XPS spectra of NFPP-Mg5% at fresh, charged and discharged states; c) CV curves of NFPP-Mg5% at different scan rates; d) CV curves of NFPP-Mg5% at 0.2 mV s^{-1} with the calculated capacitive current contribution shown by the gray shaded region; e) Capacitive capacity contribution ratios of NFPP-0 and NFPP-Mg5% at different scan rates.

shift is detected in the in situ XRD patterns without the appearance of new peak. This demonstrates that the sodium storage process of NFPP-Mg5% only involves single-phase reaction, which is consistent with the reported sodium storage mechanism of NFPP-based cathode materials.[24–26,42] Meanwhile, the ex situ XRD patterns (Figure S17, Supporting Information) correspond well with in situ XRD results. In addition, ex situ XPS spectra were obtained to reveal the chemical state change of NFPP-Mg5% during charge/discharge (Figure 3b). In the XPS spectrum of NFPP-Mg5% at fresh state, the binding energy of Fe $2p_{3/2}$ peak is 711.4 eV. For charged NFPP-Mg5%, the binding energy of Fe $2p_{3/2}$ peak increases to 712.4 eV, confirming the oxidation of Fe^{2+} to Fe^{3+} in NFPP-Mg5% during the charge process. Moreover, the binding energy of Fe $2p_{3/2}$ peak decreases to 711.1 eV in the Fe 2p XPS spectrum of NFPP-Mg5% at discharged state, indicating the reduction of Fe^{3+} to Fe^{2+} during the discharge process. Such oxidation state change of Fe during the charge/discharge process is match well with the previous literatures.[24,25,32] In summary, the sodium storage mechanism of NFPP-Mg5% is demonstrated as single-phase intercalation/deintercalation reaction accompanying with the transformation between Fe^{3+} and Fe^{2+}.

In addition, the electrochemical sodium storage behavior of NFPP-Mg5% was further analyzed by multi-scan rate CV experiment. The multi-scan rate CV curves of NFPP-Mg5% are displayed in Figure 3c. Based on these results, the diffusion-controlled and capacitive capacity contributions of NFPP-Mg5% at a fixed potential (V) were calculated according to following equation:[57–59]

$$i(V) = k_1 v + k_2 v^{1/2} \tag{2}$$

where the $k_1 v$ and $k_2 v^{1/2}$ components represent the capacitive and diffusion-controlled capacity contributions, respectively, and v is the scan rate. The calculated capacitive capacity contribution of NFPP-Mg5% increase from 72.8% to 86.1% when scan rate change from 0.2 to 1.0 mV s^{-1} (Figure 3d,e; Figure S18, Supporting Information). Combined with the in situ XRD and ex situ XPS results, it can be concluded that the sodium-ion storage process of NFPP-Mg5% is dominated by the intercalation pseudocapacitve mechanism. Meanwhile, the capacitive capacity contributions of NFPP-0 were also evaluated based on the multi-scan rate CV curves (Figure S19, Supporting Information). Compared to NFPP-0, NFPP-Mg5% displays enhanced intercalation pseudocapacitance (Figure 3e), which is responsible for the enhanced rate capability and the excellent cycling stability. Meanwhile, the diffraction peaks of NFPP-Mg5% maintain well even after long-term cycling process (Figure S20, Supporting Information), demonstrating the excellent structure stability.

To further demonstrate the potential of NFPP-Mg5% in practical application, the full SIBs based on NFPP-Mg5% and hard carbon (**Figure 4**a) were assembled. The characterization results of hard carbon used are displayed in Figure S21 (Supporting Information). The full SIB displays an initial capacity of 77.5 mAh g^{-1} (based on the mass of NFPP-Mg5%) at 500 mA g^{-1}, which remains 50 mAh g^{-1} after 200 cycles (Figure 4b). However, the average working voltage of full SIB is <2.5 V (Figure 4c), which is far from the expected value (≈3.0 V). That is ascribed to the poor electrochemical performance of hard carbon anode when using 1 M NaPF$_6$/propylene carbonate with fluoroethylene carbonate (NaPF$_6$/PC+5%FEC) electrolyte (Figure S22a,b, Supporting Information), i.e., the electrolyte used in evaluating
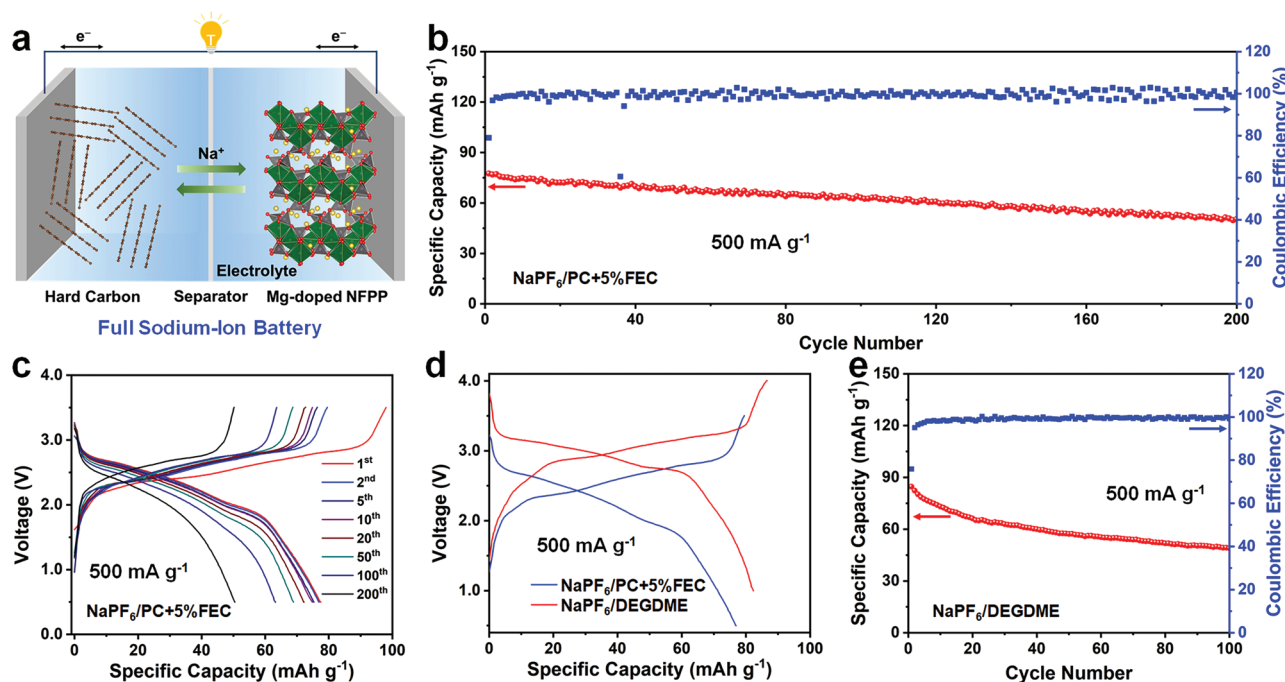
Figure 4. Full sodium-ion battery. a) Schematic illustration of full SIB based on NFPP-Mg5% cathode and hard carbon anode, b) cycling perofrmane and c) corresponding charge/discharge curves of full SIB using NaPF$_6$/PC+5%FEC electrolyte, d) the 2nd charge/discharge curves of full SIB using different electrolytes, e) cycling performance of full SIB using NaPF$_6$/DEGDME electrolyte at 500 mA g^{-1}.

the electrochemical performance of NFPP-Mg5%. In $NaPF_6$/PC+5%FEC electrolyte, the hard carbon displays low reversible capacity of below 125 mAh g^{-1}, and the charge/discharge plateau at $\approx$0.1 V is absent (Figure S22a,b, Supporting Information). In contrast, hard carbon anode displays a high capacity of 269 mAh g^{-1} with long charge/discharge plateau at $\approx$0.1 V when using ether-based electrolyte, 1 M $NaPF_6$/diethylene glycol dimethyl ether ($NaPF_6$/DEGDME) (Figure S22c,d, Supporting Information). The difference in electrochemical performance of hard carbon results from the large difference in charge transfer kinetics originated from the different composition of solid electrolyte interphase in these two electrolyte.[60] Moreover, NFPP-Mg5% cathode also displays excellent electrochemical performance in the $NaPF_6$/DEGDME electrolyte (Figure S23, Supporting Information). Therefore, the full SIB using $NaPF_6$/DEGDME electrolyte displays higher working voltage compared to the full SIB using $NaPF_6$/PC+5%FEC electrolyte (Figure 4d). In addition, the discharge medium voltage of full SIB using $NaPF_6$/DEGDME electrolyte rises from 2.84 to 2.9 V in the first few cycles and stabilize at 2.9 to 3.0 V during the subsequent cycles (Figure S24, Supporting Information). Unfortunately, the capacity of full SIB using $NaPF_6$/DEGDME electrolyte fades to 49 mAh g^{-1} after 100 cycles (Figure 4e), which is relatively worse than that of full SIB using $NaPF_6$/PC+5%FEC electrolyte. We believe that the electrochemical performance of full SIBs based on NFPP-Mg5% can be further improved when using more suitable anode material and electrolyte.

3. Conclusion

The Mg-doped NFPP/C composites were successfully synthesized and the NFPP-Mg5% exhibited highly enhanced rate performance ($\approx$40 mAh g^{-1} at 20 A g^{-1}) and ultra-long cycling life (14 000 cycles at 5 A g^{-1}). The kinetic analysis results reveal that the Mg doping improves the Na-ion diffusivity and reduces the interfacial charge transfer resistance. In addition, the sodium storage process of NFPP-Mg5% is dominated by the intercalation pseudocapacitive mechanism and the proportion of capacitive capacity is improved by Mg doping. The enhanced electrochemical kinetics and intercalation pseudocapacitance of NFPP-Mg5% is responsible for the enhanced rate performance and ultra-long cycling life. Besides, the full SIBs based on NFPP-Mg5% were assembled and displayed the discharge capacity of $\approx$50 mAh g^{-1} after 200 cycles at 500 mA g^{-1}. We believe that NFPP-Mg5% is a promising cathode material for SIBs and this work is helpful for the development of low-cost and high-performance SIBs.

Supporting Information

Supporting Information is available from the Wiley Online Library or from the author.

Acknowledgements

Conflict of Interest

The authors declare no conflict of interest.

Data Availability Statement

The data that support the findings of this study are available from the corresponding author upon reasonable request.

Keywords

[1] D. Larcher, J. M. Tarascon, *Nat. Chem.* **2015**, *7*, 19.
[2] B. Dunn, H. Kamath, J. M. Tarascon, *Science* **2011**, *334*, 928.
[3] Z. Yang, J. Zhang, M. C. Kintner-Meyer, X. Lu, D. Choi, J. P. Lemmon, J. Liu, *Chem. Rev.* **2011**, *111*, 3577.
[4] Y. Fang, Z. Chen, L. Xiao, X. Ai, Y. Cao, H. Yang, *Small* **2018**, *14*, 1703116.
[5] R. Usiskin, Y. Lu, J. Popovic, M. Law, P. Balaya, Y.-S. Hu, J. Maier, *Nat. Rev. Mater.* **2021**, *6*, 1020.
[6] F. Xiong, S. Tan, Q. Wei, G. Zhang, J. Sheng, Q. An, L. Mai, *Nano Energy* **2017**, *32*, 347.
[7] N. Yabuuchi, K. Kubota, M. Dahbi, S. Komaba, *Chem. Rev.* **2014**, *114*, 11636.
[8] T. Jin, H. Li, K. Zhu, P. F. Wang, P. Liu, L. Jiao, *Chem. Soc. Rev.* **2020**, *49*, 2342.
[9] T. Yuan, Y. Wang, J. Zhang, X. Pu, X. Ai, Z. Chen, H. Yang, Y. Cao, *Nano Energy* **2019**, *56*, 160.
[10] F. Xiong, Q. An, L. Xia, Y. Zhao, L. Mai, H. Tao, Y. Yue, *Nano Energy* **2019**, *57*, 608.
[11] Y. Liu, N. Zhang, F. Wang, X. Liu, L. Jiao, L.-Z. Fan, *Adv. Funct. Mater.* **2018**, *28*, 1801917.
[12] P. P. Prosini, C. Cento, A. Masci, M. Carewska, *Solid State Ionics* **2014**, *263*, 1.
[13] M. Avdeev, Z. Mohamed, C. D. Ling, J. Lu, M. Tamaru, A. Yamada, P. Barpanda, *Inorg. Chem.* **2013**, *52*, 8685.
[14] K. Zaghib, J. Trottier, P. Hovington, F. Brochu, A. Guerfi, A. Mauger, C. M. Julien, *J. Power Sources* **2011**, *196*, 9612.
[15] P. Barpanda, G. D. Liu, C. D. Ling, M. Tamaru, M. Avdeev, S. C. Chung, Y. Yamada, A. Yamada, *Chem. Mater.* **2013**, *25*, 3480.
[16] H. Kim, R. A. Shakoor, C. Park, S. Y. Lim, J.-S. Kim, Y. N. Jo, W. Cho, K. Miyasaka, R. Kahraman, Y. Jung, J. W. Choi, *Adv. Funct. Mater.* **2013**, *23*, 1147.
[17] Y. Kawabe, N. Yabuuchi, M. Kajiyama, N. Fukuhara, T. Inamasu, R. Okuyama, I. Nakai, S. Komaba, *Electrochem. Commun.* **2011**, *13*, 1225.
[18] J. Zhang, X. Zhou, Y. Wang, J. Qian, F. Zhong, X. Feng, W. Chen, X. Ai, H. Yang, Y. Cao, *Small* **2019**, *15*, 1903723.

**ADVANCED
SCIENCE NEWS**

www.advancedsciencenews.com

**ADVANCED
FUNCTIONAL
MATERIALS**

www.afm-journal.de

[19] Y. Cao, Y. Liu, D. Zhao, X. Xia, L. Zhang, J. Zhang, H. Yang, Y. Xia, *ACS Sustainable Chem. Eng.* **2019**, *8*, 1380.

[20] R. Rajagopalan, B. Chen, Z. Zhang, X. L. Wu, Y. Du, Y. Huang, B. Li, Y. Zong, J. Wang, G. H. Nam, M. Sindoro, S. X. Dou, H. K. Liu, H. Zhang, *Adv. Mater.* **2017**, *29*, 1605694.

[21] M. Chen, L. Chen, Z. Hu, Q. Liu, B. Zhang, Y. Hu, Q. Gu, J. L. Wang, L. Z. Wang, X. Guo, S. L. Chou, S. X. Dou, *Adv. Mater.* **2017**, *29*, 1605535.

[22] M. Chen, Q. Liu, S. W. Wang, E. Wang, X. Guo, S. L. Chou, *Adv. Energy Mater.* **2019**, *9*, 1803609.

[23] H. Kim, I. Park, D. H. Seo, S. Lee, S. W. Kim, W. J. Kwon, Y. U. Park, C. S. Kim, S. Jeon, K. Kang, *J. Am. Chem. Soc.* **2012**, *134*, 10369.

[24] H. Kim, I. Park, S. Lee, H. Kim, K.-Y. Park, Y.-U. Park, H. Kim, J. Kim, H.-D. Lim, W.-S. Yoon, K. Kang, *Chem. Mater.* **2013**, *25*, 3614.

[25] M. Chen, W. Hua, J. Xiao, D. Cortie, W. Chen, E. Wang, Z. Hu, Q. Gu, X. Wang, S. Indris, S. L. Chou, S. X. Dou, *Nat. Commun.* **2019**, *10*, 1480.

[26] A. Zhao, T. Yuan, P. Li, C. Liu, H. Cong, X. Pu, Z. Chen, X. Ai, H. Yang, Y. Cao, *Nano Energy* **2022**, *91*, 106680.

[27] X. Li, Y. Zhang, B. Zhang, K. Qin, H. Liu, Z.-F. Ma, *J. Power Sources* **2022**, *521*, 230922.

[28] Y. Cao, X. Xia, Y. Liu, N. Wang, J. Zhang, D. Zhao, Y. Xia, *J. Power Sources* **2020**, *461*, 228130.

[29] X. Ma, X. Wu, P. Shen, *ACS Appl. Energy Mater.* **2018**, *1*, 6268.

[30] X. Pu, H. Wang, T. Yuan, S. Cao, S. Liu, L. Xu, H. Yang, X. Ai, Z. Chen, Y. Cao, *Energy Storage Mater.* **2019**, *22*, 330.

[31] L. M. Zhang, X. D. He, S. Wang, N. Q. Ren, J. R. Wang, J. M. Dong, F. Chen, Y. X. Li, Z. Y. Wen, C. H. Chen, *ACS Appl. Mater. Interfaces* **2021**, *13*, 25972.

[32] J. Zhang, L. Tang, Y. Zhang, X. Li, Q. Xu, H. Liu, Z.-F. Ma, *J. Power Sources* **2021**, *498*, 229907.

[33] F. Xiong, S. Tan, X. Yao, Q. An, L. Mai, *Mater. Today* **2021**, *45*, 169.

[34] Y. Zhang, L. Tao, C. Xie, D. Wang, Y. Zou, R. Chen, Y. Wang, C. Jia, S. Wang, *Adv. Mater.* **2020**, *32*, 1905923.

[35] E. Uchaker, G. Cao, *Chem. Asian J.* **2015**, *10*, 1608.

[36] F. Xiong, Y. Jiang, L. Cheng, R. Yu, S. Tan, C. Tang, C. Zuo, Q. An, Y. Zhao, J. J. Gaumet, L. Mai, *Interdiscip. Mater.* **2022**, *1*, 140.

[37] R. D. Shannon, *Acta Crystallogr. A* **1976**, *32*, 751.

[38] Y. Fei, L. Zhang, A. Corgne, H. Watson, A. Ricolleau, Y. Meng, V. Prakapenka, *Geophys. Res. Lett.* **2007**, *34*, L17307.

[39] L. Ren, L. Song, Y. Guo, Y. Wu, J. Lian, Y.-N. Zhou, W. Yuan, Q. Yan, Q. Wang, S. Ma, X. Ye, Z. Ye, J. Lu, *Appl. Surf. Sci.* **2021**, *544*, 148893.

[40] R. J. Clément, J. Billaud, A. R. Armstrong, G. Singh, T. Rojo, P. G. Bruce, C. P. Grey, *Energy Environ. Sci.* **2016**, *9*, 3240.

[41] H. Li, X. Yu, Y. Bai, F. Wu, C. Wu, L.-Y. Liu, X.-Q. Yang, *J. Mater. Chem. A* **2015**, *3*, 9578.

[42] X. Wu, G. Zhong, Y. Yang, *J. Power Sources* **2016**, *327*, 666.

[43] Q. Huang, S. J. Hwu, *Inorg. Chem.* **1998**, *37*, 5869.

[44] T. Jawhari, A. Roid, J. Casado, *Carbon* **1995**, *33*, 1561.

[45] F. Xiong, F. Lv, C. Tang, P. Zhang, S. Tan, Q. An, S. Guo, L. Mai, *Sci. China Mater.* **2020**, *63*, 1993.

[46] A. Sadezky, H. Muckenhuber, H. Grothe, R. Niessner, U. Pöschl, *Carbon* **2005**, *43*, 1731.

[47] M. J. Aragón, P. Lavela, R. Alcántara, J. L. Tirado, *Electrochim. Acta* **2015**, *180*, 824.

[48] T. Jawhari, A. Roig, J. Casado, *Carbon* **1995**, *33*, 1561.

[49] B. Dippel, H. Jander, J. Heintzenberg, *Phys. Chem. Chem. Phys.* **1999**, *1*, 4707.

[50] X. Ma, Z. Pan, X. Wu, P. K. Shen, *Chem. Eng. J.* **2019**, *365*, 132.

[51] N. V. Kosova, V. A. Belotserkovsky, *Electrochim. Acta* **2018**, *278*, 182.

[52] M. Gaberscek, J. Moskon, B. Erjavec, R. Dominko, J. Jamnik, *Electrochem. Solid-State Lett.* **2008**, *11*, A170.

[53] R. Ruffo, R. Fathi, D. J. Kim, Y. H. Jung, C. M. Mari, D. K. Kim, *Electrochim. Acta* **2013**, *108*, 575.

[54] G. Longoni, J. E. Wang, Y. H. Jung, D. K. Kim, C. M. Mari, R. Ruffo, *J. Power Sources* **2016**, *302*, 61.

[55] J. Moškon, J. Žuntar, S. Drvarič Talian, R. Dominko, M. Gaberšček, *J. Electrochem. Soc.* **2020**, *167*, 140539.

[56] M. Gaberscek, *Nat. Commun.* **2021**, *12*, 6513.

[57] C. Choi, D. S. Ashby, D. M. Butts, R. H. DeBlock, Q. Wei, J. Lau, B. Dunn, *Nat. Rev. Mater.* **2019**, *5*, 5.

[58] T. C. Liu, W. G. Pell, B. E. Conway, S. L. Roberson, *J. Electrochem. Soc.* **1998**, *145*, 1882.

[59] J. Wang, J. Polleux, J. Lim, B. Dunn, *J. Phys. Chem. C* **2007**, *111*, 14925.

[60] H. S. Hirsh, B. Sayahpour, A. Shen, W. Li, B. Lu, E. Zhao, M. Zhang, Y. S. Meng, *Energy Storage Mater.* **2021**, *42*, 78.